RSC Advances

ROYAL SOCIETY OF CHEMISTRY

www.rsc.org/advances

Formation of short three dimensional porous assemblies of super hydrophobic acetylene black intertwined by copper oxide nanorods for robust counter electrode of DSSCs

Waqar Ahmad[a], Liang Chu[a], Majid Raissan Al-bahrani[a], Zhichun Yang[a], Siliang Wang[a], Li Luying[a], Yihua Gao*[ab]

[a]Center for Nanoscale Characterization & Devices (CNCD), Wuhan National Laboratory for Optoelectronics (WNLO) & School of Physics, Huazhong University of Science and Technology (HUST), Luoyu Road 1037, Wuhan 430074, China

[b]Hubei Collaborative Innovation Center for Advanced Organic Chemical Materials, 368 Youyi Avenue, Wuhan 430062, China

Abstract

In this study, we synthesized monolithic copper-oxide nanorods (CuO-NRs) and doped into active super hydrophobic acetylene black (AB) nanocrystals *via* fast solvation method. The developed short-dimension assemblies are utilized as counter electrode (CE) materials for energy harvesting in dye sensitized solar cells (DSSCs). Cyclic voltammetry and electrochemical impedance spectroscopy analyses reveal that the hybrid (CuO-NRs/AB) CE display fast reduction rate of I_3^- and boost holes-cascading as comparing to those of individual AB CE, due to superior catalytic characteristics of CuO-NRs and good electrical conductivity of AB. The CuO-NRs/AB based DSSCs exhibits an enhanced power conversion efficiency (PCE) of 8.05%, in contrast to AB (6.51%) and pristine Pt (6.96%) CEs based DSSCs under same experimental conditions. The CuO-NRs/AB CE, along with impressive results renders their prospective applications in robust DSSCs.

Keywords: CuO nanorods, acetylene black, counter electrode and dye-sensitized solar cells.

1. Introduction

Dye-sensitized solar cells (DSSCs) have appeared to be a promising prospective applicant among all other photovoltaic techniques due to shortage of energy resources and environmental pollution problems. DSSCs convert solar-to-electrical energy by an efficient and facile eco-friendly manner.[1,2] Traditionally, standard DSSC device is the combination of working electrode, dye molecules, a spacer, electrolyte solution and counter electrode (CE).[3] As a key component of DSSCs, CE should retain minimum resistance, outstanding catalytic property and high current density to build a complete circuit.[4] Owing to the high conductivity and good electro-catalytic activity, the most favorable CE material in DSSCs is Pt. However, Pt is noble and scarce earth element that leads significantly high price in the market.[5,6] Therefore, it is essential to develop a cost effective CE for DSSCs.

In the past decades, several viable substitutes of Pt such as carbon based materials, conducting polymers and transition metal containing constituents have been reported as potential CEs materials in DSSCs.[7] Among them, carbonaceous materials have shown quite promising and remarkable performance but their conversion efficiency is still insufficient compared to that of Pt. Although, these materials possess significantly high electrical conductivity but due to low catalytic activity, capacitance and chemical stability in iodine based electrolytes solution, it is hard to use as CE in DSSCs.[8,9] On the other hand, transition metal oxides show desirable features such as high catalytic, capacitance and better stability characteristics in I_3^-/I^- electrolyte, however, these have poor electronic conductivity and low ion diffusion rate.[10,11] Therefore combining carbonaceous and transition metal oxide material with low dimension has been an effective strategy for DSSCs materials.[12,13]

The four main classifications of composite structure have been examined until now. These composites i) are made by the mixture of carbon species and oxide based materials physically.[14,15] ii) have cable-like structure fabricated by coating conducting rods or wire with active oxide species.[16,17] iii) have interpenetrative network structure of carbonaceous materials.[18,19] and iv) have sandwich like configuration rather loading layers of graphene and oxide materials.[20,21] All these composites based structures DSSCs retain different characteristics in terms of ion and charge transportation and showed distinct performances.

However, their extensive efforts for designing new materials in the outline above four synthetic methods still have shortcomings, e.g. In composite i): the transport pathways for ions and charges are usually incompetent and poor controlled due to the irregular mixing of binding oxides and carbonaceous species. ii): the cable-like structure locally provides easiest way for charge transportation but the oxide coated layer increases the CNTs contact resistance, which strongly affect the cells performance.[14] iii): interpenetrative network of carbon based composite delivers excellent performances but reduces the stability of electrode and composite iv): the sandwich like structure composite makes intimate contact between carbonaceous materials and active oxides, as a result the two-dimensional structure inhibits the charge transport as well as three-dimensional mass.

In this work, we report the fabrication of novel class nanocomposite architecture with the aim of increasing efficiency of DSSCs by very simple and efficient solution process. Unlike the above mentioned approaches, our strategy is based on fast solvation process that uses hydrophobic materials directly. As illustrated in Fig. 1, first we used nonpolar solvents for dispersion of hydrophobic materials and secondly with addition of polar solvents, all

hydrophobic nanocrystals accumulate around the hydrophobic nanorods and gain organized shaped assemblies. However, calcination creates pores in these 3-D assemblies.

In our experiment, we used acetylene black (AB) nanocrystals with building block copper oxide nanorods (CuO-NRs) as a conceptual model. AB has high conductivity, low cost and energy storage material while CuO is p-type semiconductor facilitates holes conduction and also provides intertwined structure to the nanocomposite. First we dispersed hydrophobic AB nanocrystals and CuO-NRs[22,23] in toluene and then with addition of methanol both hydrophobic nanocrystals and nanorods were assembled. However, by calcination composite assemblies become porous for robust CEs. Our developed 3-D short structure provides distinctive characteristics which are necessary for high performance CE of DSSCs by following means. The short closely packed structures not only contact the oxides and AB nanoparticles locally for holes conduction but also offer excellent network for whole electrode. The porous structure facilitates effective channel for iodine based electrolyte transportation and active framework offers reduced ion-diffusion length. Therefore, it comprises excellent chemical and mechanical robustness which is necessary for stable CEs.

The state-of-the-art, our electrochemical and structural properties specify that the as prepared AB/CuO-NRs CEs should be capable of working efficiently as conventional Pt CE. In particular, the obtained power conversion efficiency (PCE) of CuO-NRs/AB under standard illumination condition (1.5G, 100mW cm^{-2}) was 8.05%, which indicates promising potential application for electrodes in DSSCs. Here we propose that the high performance of CuO-NRs/AB based DSSCs is associated with effective synthesis of low dimensional assemblies.

2. Experimental

2.1 Reagents and materials

All chemicals and reagents were of analytical grade and used without any additional purification. Copper(II) chloride dihydrate ($CuCl_2.2H_2O$), sodium hydroxide (NaOH), ethanol (C_2H_6O), terpineol ($C_{10}H_{18}O$), titanium tetrachloride ($TiCl_4$), ethyl cellulose, tetrabutyl titanate ($C_{16}H_{36}O_4Ti$) and acetic acid (HAc) were purchased from Sinopharm Chemical Reagent Co., Ltd. Acetylene (99%) was obtained from Hubei Chuchengwei Chemical Co., Ltd. N719 (cis–bis (isothiocyanato) bis(2,2'-bipyridyl-4,4'-dicarboxylato) ruthenium(II) bis-tetrabutylammonium) was supplied by Solaronix. Fluorine doped tin oxide glass (FTO, 7 Ω cm^{-2}) was purchased from Nippon Sheet Glass Co., Ltd. and washed ultrasonically with laundry soap, acetone, Milli-pore water (18.2 MΩ-cm) and ethanol for 15 minutes, respectively. Lithium iodide (LiI, 99.999%), iodine (I_2, 99.99%), $TiCl_4$. $3H_2O$ (99.99%), 1-methyl-3-propylimidazolium iodide (PMII, 98%), 4-tert-butylpyridine (4-TBP, 96%) and tert-butyl alcohol (99.5 %) were obtained from Aladdin. Acetonitrile (99.8%) and valeronitrile (99%) were bought from Alfa Aesar.

2.2 Preparation of materials

CuO nanorod formation: In a typical procedure, first 0.10 g $CuCl_2.2H_2O$ (as copper source) was dispersed in the mixture of 15 mL ethanol and 30 mL distilled water under agitation. After 10 min, 0.55 g solid NaOH particles were directly added and the solution got deep-blue color. Afterward, the total volume of reagents is adjusted to 100 mL by adding distilled water. The crude solution $Cu(OH)_2$ was separated by centrifugation (at 1600 rpm for 5 min) and decantation, washed with distilled water and ethanol, respectively. The resultant blue precipitate $Cu(OH)_2$ was dried overnight at 60 °C and the color turned black which is feasible symptom of CuO.

Finally to obtain the purified black target hydrophobic CuO nanorods, the dried CuO transition state was heated at 400 °C for 2 h in air.

AB nanoparticle formation: The AB was prepared by the pyrolysis route.[24] Typically, 1.5 g acetylene (C_2H_2) was heated at 680 °C in Ar atmosphere for 2 h and cooled down to room temperature naturally to get the super hydrophobic AB nanoparticles (size about 40 nm) with porous structure.

Synthesis of CuO-NRs/AB nanocomposites: The nanocomposite was prepared by reacting 25 mL toluene solution and 250 mg AB nanocrystals at room temperature for 1 h with stirring. Then 40 mg CuO nanorods were dispersed in above solution under ultrasonication and stirred. Next to induce short-dimensions assemblies, 35 mL methanol were added into the mixture and stirred. Solid/liquid separation was done by centrifugation. Finally the wet products were dried at 60 °C overnight and then annealed at 400 °C for 2 h in muffle furnace.

2.3 Preparation of counter electrode

The following experimental procedure was adopted for the feasibility of synthesizing hybrid CuO-NRs/AB CEs: 1.0 g synthesized nanocomposite, 0.2 mL acetic acid, 0.50 g ethyl cellulose, 3.0 g terpineol anhydrous and 10 mL ethanol were mixed together in 25 mL beaker by tempestuously agitation at room temperature to attain fine dispersion. After vigorous agitation, the reactant was grounded in a mortar and used ultrasonication for 15 min. Subsequently, the composite slurry was deposited by mean of doctor-blading method onto patterned conducting layer of FTO glass. The resultant layer was gradually heated at 400 °C for 2 h to remove the residual organic contents and formed network of 3-D structure using muffle furnace. As

reference, AB CE was also prepared according to the above experimental approach without existence of CuO constituents and the conventional Pt CE was prepared as stated by literature [25].

2.4 Fabrication of DSSCs

The mesoporous TiO_2 suspension was synthesized by the modified process reported literature.[26,27] In brief, 10 mL tetrabutyl titanate and 15 mL ethanol were mixed together in 100 mL beaker under vigorous stirring at room temperature. Next, 10 mL acetic acid and 40 mL distilled water were added into the above solution. After 1 h continuous stirring, the hydrothermal treatment of the solution were carried out at 200 °C for 12 h. Solid/liquid was separated by centrifugation and the precipitate washed with distilled water and ethanol three times. Finally, the obtained TiO_2 dried at 80 °C for whole night in air oven. Next to acquire fine suspension, 1.5 g as-prepared TiO_2 was mixed with 12 mL ethanol and 0.4 mL acetic acid added drop wise under magnetic stirring. After 10 min, 0.8 g ethyl cellulose and 0.5 g terpineol as binder and surfactant were added to the above solution respectively under continuous stirring at room temperature. After agitation, white slurry was grounded in mortar and ultrasonicated for 15 min respectively. For compact layer of TiO_2, the already cleaned conducting FTO plate was immersed into 40 mM $TiCl_4$ aqueous solution at 70 °C in air oven for 0.5 h. Subsequently, the layer of 20 nm sized TiO_2 was coated onto the treated substrate by doctor-blade method, using one layer of magic scotch tape yielding film thickness of ~7 μm and sintered at 130 °C for 0.5 h. With initial drying, the TiO_2 film color turns into light brown/yellow. To obtain a light scattering layer, 200 nm sized TiO_2 single layer having thickness of ~4 μm was then deposited on the synthesized FTO plate. For the removal of organic materials the as-prepared film was sintered at 450 °C for 15 min and next post treated at 500 °C for 1 h in muffle furnace. After thermal annealing, color of the double layer TiO_2 film was changed into milky and finally the as-

prepared sample was treated with $TiCl_4$ aqueous solution. Before dipping into dye solution, the prepared sample was re-calcined in furnace at 520 °C for 0.5 h and then slowly cooled to 80 °C. Finally for dye sensitization, the two layers TiO_2 electrode was soaked into 0.5 mM N719 dye in acetonitrile/tert-butanol solution (V:V/1:1) for 20 h at room temperature. To remove the physically adsorbed dye molecules the treated sample rinsed thoroughly with ethanol and allowed in air to dry. The resulting DSSCs were assembled by using dye sensitized photoanode electrode, electrolyte solution and counter electrode. The electrolyte was composed of 0.6 M PMII, 0.05 M LiI, 0.03 M I_2, 0.1 M GuSCN and 0.5 M 4-TBP in acetonitrile and valeronitrile (V:V/85:15) as solvents. The projected area of the solar cell was controlled to be 0.15 cm^2 without mask.

2.5 Characterization

X-ray diffraction (XRD, PANalytical B.V. Netherland, radiation wavelength 1.54060 Å) system furnished with Cu-K-alpha radiation was used to study crystalline structures of the as-synthesized samples. The surface morphologies and nano-composite structures of the samples were investigated by a field emission scanning electron microscopy (FE-SEM, FEI NOVA NanoSEM 450), Transmission electron microscopy (TEM, FEI Tecnai G^2 20 UTwin) and Raman spectroscopy (HORIBA Jobin Yvon UV-VIS-NIR LabRAM, 532 nm). Energy-dispersive X-ray spectroscopy (EDS) equipped with FE-SEM was carried out for observation of various elements in the prepared films.

2.6 Electrochemical measurements

The photocurrent density versus voltage (J-V) curves was measured under dark and illumination coming from a solar simulator (Newport, USA) with AM 1.5G (100 mW cm^{-2}).

Electrochemical impedance spectroscopy (EIS) measurements were recorded using an Auto-lab electrochemical workstation (model AUT84315, the Netherlands). Cyclic voltammetry (CV) measurement was carried out in a three-electrode system using a CHI660C potentiostate with a platinum electrode and Ag/AgCl were used as a counter electrode and reference electrode at scan rate of 50 mVs^{-1} in acetonitrile solution containing 1 mM I_2, 10 mM LiI, and 100 mM $LiClO_4.3H_2O$.

3 Results and Discussion

3.1 Material characteristics

Fig. 2(a) shows the as-synthesized powders X-Ray diffraction (XRD) pattern of AB, CuO-NRs and CuO-NRs/AB nanocomposites. In undoped AB, the diffraction patterns depict partially graphitized structure of acetylene black and can be readily indexed to reference patterns (PCPDFWIN, file No. 75-2078), representing that AB sample is complex carbon materials. All the XRD reflection peaks of CuO nanorods are indexed and well matched with monoclinic structure of CuO file (PCPDFWIN, file No. 45-0937). Figure 2(a) shows the magnified XRD pattern of CuO-NRs doped AB sample revealing the presence of CuO. There is no characteristic peaks of any impurities such as Cu_2O, $Cu(OH)_2$, or precursors used are observed, demonstrating the formation of a pure CuO phase. The EDX analysis Fig. 2(b, c & d) shows no other elements are detectable in the above samples.

The surface morphology of nanocomposite CuO-NRs/AB CEs are characterized by FE-SEM. Fig. 3(a) presents the SEM image of AB nanoparticles, prepared by pyrolysis method. The as-prepared nanocrystals show uniform porous structure characteristics with particle size ~40 nm. Fig. 3(b) shows representative image of individual CuO nanorods used for building 3-D low

dimensions assemblies. The SEM micrograph also reveals the length and diameter of as-prepared CuO nanorods, about 200 nm and 40 nm respectively. Fig. 3(c) shows the plan-view FE-SEM images of CuO-NRs/AB composite where the circled regions demonstrate the 3D well-connected structure of hydrophobic AB nanoparticles and CuO nanorods. The inset in Fig. 3(c) shows the cross section micrograph of CE, indicating the thickness of porous film is about 11.7 μm. Overall these short-dimension assemblies are uniformly distributed on FTO substrate and provide local path ways for iodide/triiodide electrolyte, thus accelerate charge transportation. Fig. 3(d) depicts the high resolution SEM image of as-prepared assemblies varied from few hundred nanometers to few micrometers. The inset in Fig. 3(d) exhibits high porosity with uniform pore size distribution. Most importantly, the observed interconnected porous structure fortifies strong adhesion to FTO glass as well as favorable for penetration of redox ions into the film.

In order to study the detailed morphology and further evidence of CuO-NRs/AB composite, the sample is observed by TEM and high resolution TEM (HR-TEM). A TEM image in Fig. 3(e) shows the short-dimension intertwined network of both hydrophobic materials which might be beneficial for holes transportation. Fig. 3(f) shows the selected area electron diffraction (SAED) pattern of AB nanocrystals indicating the fringe spacing of 0.334 nm, which matches well with the inter-planar spacing of (111) planes of the reference (PCPDFWIN, file No. 75-2078). Fig. 3(g) illustrates the electron diffraction pattern of a CuO nanorod revealing [310] zone axis, portraying that the nanorod is single crystalline.[28] The lattice image with inset of CuO nanorod in Fig. 3(h) depicts the interplanar distance of *ca.* 0.253 nm attributed to (002) plane of monoclinic-phase CuO with reference (PCPDFWIN, file No 45-0937).

Beside surface analysis, both samples are characterized by Raman spectroscopy for structural changes. The observed Raman spectra of all samples demonstrate two broad peaks as

shown in Fig. 4(a). The peaks intensity at wave number 1344 cm^{-1} and 1580 cm^{-1} correspond to D-band of disordered carbons and G-band of graphitic carbons, respectively.[29] Since relative intensity ratio of I_D/I_G is ruler of graphitization degree, the corresponding I_D/I_G ratio values 1.14 of AB and 1.22 of CuO-NRs/AB indicates that graphitization of AB is decreased in the presence of CuO nanorods. This result can be attributed to the fact that some surface imperfects or defects are attached with graphitic AB, resulting in the disorder degree.[30] Therefore, these added active sites justify the use of defected AB doped with CuO-NRs as an efficient CE material in DSSCs.

3.2 Electrocatalytic behavior

The catalytic performances are responsible for different properties of DSSCs and studied by various techniques. Three electrode cyclic voltammetry is conducted to evaluate the electrocatalytic activity of various CEs for the reduction of triiodide into iodide. Notably, the cathodic current density is strongly dependent on the scan rate of CV measurements.[31] Fig 4(b) shows the CV curves of different CEs over potential range from -1.5 V to 1.5 V with scan rate of 50 mV s^{-1}. As expected, there are two well resolved redox pair peaks has been observed, i.e low potential range corresponding to I^-/I_3^- and high potential range correspond to I^-/I_2^-. Two critical parameters influence the DSSCs performance i.e. peak current density and peak-to-peak separation (E_{pp}). Apparently, the CuO-NRs/AB CE exhibits slightly larger redox peak current density and lower peak-to-peak separation (shown in Table 1) than those of individual AB electrode. The higher background current response of CuO-NRs/AB CE is mainly due to the capacitance of effective diffusion on electrode/electrolyte interface that promote the adsorption and desorption of I^-/ I_3^- redox shuttle. This phenomenon could support the electrocatalytic activity towards the I_3^- reduction. However, AB electrodes indicating poor catalytic activity due to its graphitization structure which limits the sufficient defective sites of amorphous carbon and

disorder mesoporous channels, confirmed by our Raman analysis. Moreover, the other key parameter (E_{pp}) exhibits the reversibility of the CEs. With the introduction of CuO-NRs to AB, the CuO-NRs/AB shows smaller E_{pp} value and faster reduction reaction than that of AB and reference Pt electrodes, which is due to high electrical conductivity of AB and high catalytic activity character of CuO-NRs. So the smaller E_{pp} value indicates excellent catalytic reversibility towards the reduction of I_3^- that CuO-NRs/AB CE has. Moreover, the reduction peaks of AB and Pt is more negative than CuO-NRs/AB electrode, implying more irreversible process for the triiodide reduction.[27] This demonstrates that the CuO-NRs/AB CE with corresponding CuO contents exposed superb catalytic activity towards the I_3^- reduction and a good photovoltaic performance of the cells.

Electrochemical impedance spectroscopy (EIS) is another well-known effective test to evaluate the electrocatalytic behavior of different CEs. The obtained Nyquist plots with inset equivalent circuit are shown in Fig. 4(c) and their respective parameters are listed in Table 1. In a typical Nyquist plot, the intercept of the 1st semicircle within high frequency range (10^6~10^5 Hz) on real axis represents the series resistance (R_s) which is related to the sheet resistance of FTO glass, contact resistance of the cell and resistance of external circuit. The charge transfer resistance (R_{ct}) obtained from 1st semicircle in high frequency range is assigned to the C.E/electrolyte interface. The 2nd semicircle in intermediate frequency range ascribes electrons transport resistance at photoelectrode/dye/electrolyte interface. Usually the R_s and R_{ct} values are adopted to evaluate the resistance and intrinsic catalytic activity of electrodes.[32] The R_s values are found nearly similar for all CEs, which are related to FTO glass and R_{ct} values for CuO-NRs/AB, AB and Pt CEs are 1.9 Ω, 2.1 Ω and 3.45 Ω respectively. The CuO-NRs/AB CE exhibits lower R_{ct} value than those of AB and Pt CEs indicating excellent electrocatalytic activity.

The superb catalytic activity also confirms the supremacy of unique low-dimension structure of CuO-NRs/AB on the triiodide reduction. On one hand due to the intertwined porous structure of low dimensions, CuO-NRs provide fast ion transport network and suitable graphitization degree which are advantageous for electron transportation. On the other hand, the definite synergistic effect among highly distributed AB nanoparticles and CuO-NRs can significantly limits the electron transfer resistance, yielding in a substantial enhancement of the catalytic activity. The EIS results of DSSCs are in good agreement with the cyclic voltammetry experiments.

3.4 Photovoltaic performance

The influence of electrocatalytic characteristics on the photovoltaic performance is examined by fabricating DSSCs with CuO-NRs/AB and AB CEs, and subsequently compared with Pt based DSSCs. Fig 4(d) shows the J-V (current density *versus* voltage) curves of sandwich type DSSCs fabricated with different CEs under dark and standard illumination. The derived photovoltaic parameters such as short-circuit current density (J_{sc}), open-circuit voltage (V_{oc}) and fill factor (FF) with their relative efficiencies (η) are summarized in Table 1. Literally, the I_3^-/I^- reduction reaction on the interface of electrocatalyst could be affected by these three fundamental factors i.e. diffusion of electrolyte, electron transport and catalytic active sites. The best catalytic activity must be the favorable combination of above three factors.

CuO-NRs/AB depicts superior PCE (8.05%) over pristine AB (6.51%) and Pt (6.96%) due to the above stated basic parameters i.e. J_{sc}, V_{oc} and FF, which are explained subsequently. (i) Short-circuit photocurrent: CuO-NRs/AB (15.94 mA cm^{-2}) shows higher J_{sc} than those of pristine AB (14.84 mA cm^{-2}) and Pt (15.25 mA cm^{-2}). The low J_{sc} of AB and Pt are due to their poor electron conductivity. In contrast, amorphous carbon possesses more defective sites or catalytic

sites as compare to graphitic carbon.[27] So the transportation of electrons increases due to the suitable amorphous structure of amorphous carbon. The graphitic carbon (AB) modified by CuO nanorods can not only boost electrical conductivity but also provides sufficient catalytic sites.[33,34] (ii) open-circuit potential: The V_{oc} of AB (0.74 V) and Pt (0.71 V) CEs are much lower than that of CuO-NRs/AB (0.77 V) based CE DSSCs, using same working electrode and electrolyte. In fact, the open-circuit voltage is the difference of Fermi level of working electrode TiO_2 film and the redox potential of mediating agent that is influenced by instinct material properties of the CEs.[31] (iii) It is well-known that, FF is closely related to the R_s and R_{ct} of DSSCs. Here, the R_s of CuO-NRs/AB CE based DSSCs are nearly similar to those of AB and Pt CEs based DSSCs. Therefore, the superior FF might be due to the lower R_{ct} of CuO-NRs/AB CE. Both enhanced electrical conductivity and abundant active sites of CuO-NRs/AB make it attractive CEs material for high performances DSSCs.

Table 1: Photovoltaic parameters and electrochemical characteristics of DSSCs based on CuO-NRs/AB, AB, and conventional Pt CEs.

CE	J_{sc} (mA.cm^{-2})	V_{oc} (V)	FF	PCE (%)	R_s (Ω)	R_{ct} (Ω)	I_{pc} (mA.cm^{-2})	E_{pp} (V)
CuO-NRs/AB	15.94	0.77	0.65	8.05 ± 0.2	21.00	1.90	-4.117	0.4261
AB	14.84	0.74	0.60	6.51 ± 0.2	20.11	3.45	-3.875	0.5668
Pt	15.25	0.71	0.63	6.96 ± 0.2	22.59	2.10	-3.097	0.5958

4. Conclusions

Short-dimension assemblies of CuO-NRs/AB composite for high performance DSSCs are fabricated by a facile approach in the presence of non-polar and polar solvents. Based on the proposed method, CuO-NRs/AB provides low dimension 3-D assemblies architecture, specific electrocatalytic activity and high mesoporous channels for CEs, yielding higher solar-to-electrical PCE than plain AB based DSSCs. The light-to-electricity power conversion efficiency of the cell with CuO-NRs/AB CE (8.05%) is comparable to that of conventional Pt (6.96 %). It is demonstrated that the addition of CuO-NRs can enhanced the electrocatalytic activity of AB, due to the synergistic catalytic effect and increased electroconductivity of suitable graphitization degree of AB. Moreover, our proposed method of CuO-NRs/AB not only offers a novel and low

possible reduction cost pathway to robust CEs but also can expands it to other metal oxides with carbonaceous materials as an efficient CEs catalysts.

Acknowledgment

This work was supported by the National Basic Research Program (2011CB933300) of China.

References

1. R. D. Costa, F. Lodermeyer, R. Casillas and D. M. Guldi, *Energ. Environ. Sci.*, 2014, **7**, 1281-1296.
2. D. Hwang, D. Y. Kim, S.-Y. Jang and D. Kim, *J. Mater. Chem. A*, 2013, **1**, 1228-1238.
3. N. Wang, L. Han, H. He, N.-H. Park and K. Koumoto, *Energ. Environ. Sci.*, 2011, **4**, 3676-3679.
4. P. Li, H. Cai, Q. Tang, B. He and L. Lin, *J. Power Sources*, 2014, **271**, 108-113.
5. C.-Y. Wu, Y.-T. Liu, P.-C. Huang, T.-J. M. Luo, C.-H. Lee, Y.-W. Yang, T.-C. Wen, T.-Y. Chen and T.-L. Lin, *Nanoscale*, 2013, **5**, 9181-9192.
6. Z. Zheng, J. Chen, Y. Hu, W. Wu, J. Hua and H. Tian, *J. Mater. Chem. C*, 2014, **2**, 8497-8500.
7. M. Ye, X. Wen, M. Wang, J. Iocozzia, N. Zhang, C. Lin and Z. Lin, *Mater. Today*, 2014.
8. W. Sun, T. Peng, Y. Liu, N. Huang, S. Guo and X. Zhao, *Carbon*, 2014.
9. N. G. Sahoo, Y. Pan, L. Li and S. H. Chan, *Adv. Mater.*, 2012, **24**, 4203-4210.
10. X. Xin, M. He, W. Han, J. Jung and Z. Lin, *Angew. Chem. Int. Edit.*, 2011, **50**, 11739-11742.
11. M. G. Walter, E. L. Warren, J. R. McKone, S. W. Boettcher, Q. Mi, E. A. Santori and N. S. Lewis, *Chem. Rev.*, 2010, **110**, 6446-6473.
12. T. Bordjiba and D. Bélanger, *J. Electrochemic. Soc.*, 2009, **156**, A378-A384.
13. A. Asthana, T. Maitra, R. Büchel, M. K. Tiwari and D. Poulikakos, *ACS App. Mater. Interfaces*, 2014.
14. D. Jariwala, V. K. Sangwan, L. J. Lauhon, T. J. Marks and M. C. Hersam, *Chem. Soc. Rev.*, 2013, **42**, 2824-2860.

15. S. Y. Kim, Y. Kim, K. M. Lee, W. S. Yoon, H. S. Lee, J. T. Lee, S.-J. Kim, Y. H. Ahn, J.-Y. Park and T. K. Lee, *ACS App. Mater. Interfaces*, 2014, **6**, 13430-13437.

16. Z. Chen, D. Zhang, X. Wang, X. Jia, F. Wei, H. Li and Y. Lu, *Adv. Mater.*, 2012, **24**, 2030-2036.

17. H. Tang, C. M. Hessel, J. Wang, N. Yang, R. Yu, H. Zhao and D. Wang, *Chem. Soc. Rev.*, 2014, **43**, 4281-4299.

18. Z. Tian, Y. Zhou, Z. Li, Q. Liu and Z. Zou, *J. Mater. Chem. A*, 2013, **1**, 3575-3579.

19. L. Battista, L. Mecozzi, S. Coppola, V. Vespini, S. Grilli and P. Ferraro, *Appl. Energ.*, 2014, **136**, 357-362.

20. D. W. Chang, H.-J. Choi, A. Filer and J.-B. Baek, *J. Mater. Chem. A*, 2014.

21. M.-H. Yeh, L.-Y. Lin, C.-L. Sun, Y.-A. Leu, J.-T. Tsai, C.-Y. Yeh, R. Vittal and K.-C. Ho, *J. Phys. Chem. C*, 2014.

22. X. Wang, H. Zhang, J. Zhang, H. Xu, Z. Tian, J. Chen, H. Zhong, Y. Liang and B. Yi, *Electrochim. Acta*, 2006, **51**, 4909-4915.

23. N. Miljkovic, D. J. Preston, R. Enright and E. N. Wang, *App. Phy. Lett.*, 2014, **105**, 013111.

24. F. Cai, J. Chen and R. Xu, *Chem. Lett.*, 2006, **35**, 1266-1267.

25. M. Wu, X. Lin, Y. Wang, L. Wang, W. Guo, D. Qi, X. Peng, A. Hagfeldt, M. Grätzel and T. Ma, *J. Am. Chem. Soc.*, 2012, **134**, 3419-3428.

26. D. Macwan, P. N. Dave and S. Chaturvedi, *J. Mater. Sci.*, 2011, **46**, 3669-3686.

27. M. Chen, L.-L. Shao, X. Qian, T.-Z. Ren and Z.-Y. Yuan, *J. Mater. Chem. C*, 2012, **2**, 10312-10321.

28. P. Lignier, R. Bellabarba and R. P. Tooze, *Chem. Soc. Rev.*, 2012, **41**, 1708-1720.

29. H. Li, J, Chen, S. Han, W. Niu, X. Liu, G, Xu, *Talanta,* 2009, **79**, 165-170.

30. C.-T. Hsieh, B.-H. Yang and J.-Y. Lin, *Carbon*, 2011, **49**, 3092-3097.

31. S.-Y. Tai, C.-J. Liu, S.-W. Chou, F. S.-S. Chien, J.-Y. Lin and T.-W. Lin, *J. Mater. Chem.*, 2012, **22**, 24753-24759.

32. E. Ramasamy, C. Jo, A. Anthonysamy, I. Jeong, J. K. Kim and J. Lee, *Chem. Mater.*, 2012, **24**, 1575-1582.

33. V. DeGeorge, S. Shen, P. Ohodnicki, M. Andio, M.E. McHenry, *J. Electron. Mater.,* 2014, **43**, 96-108.

34. S. Shen, P.R. Ohodnicki, S.J. Kernion, and M.E. McHenry, *J. Appl. Phys.*, 2012, **112**, 103705.

35. S.-H. Hsu, C.-T. Li, H.-T. Chien, R. R. Salunkhe, N. Suzuki, Y. Yamauchi, K.-C. Ho and K. C. W. Wu, *Sci. Rep.*, 2014, **4**.

Figure Captions

Figure 1: Schematic of the fabrication procedure of 3D short assemblies for counter electrode of DSSCs.

Figure 2: (a) XRD Analysis of AB, CuO-NRs and CuO-NRs/AB nanocomposite electrodes. EDX spectra of (b) AB nanocrystals (c) CuO nanorods and (d) CuO-NRs/AB nanocomposite.

Figure 3: (a) & (b) representative SEM images of AB nanoparticles and CuO-NRs, respectively. (c) Top view surface and cross sectional (inset) SEM images of CuO-NRs/AB nanocomposite film. The circled regions illustrate the short 3D assemblies of super hydrophobic AB nanoparticles and CuO-NRs. (d) high resolution SEM image of short-dimension assembly, inset shows highly porous structure of assemblies. (e) TEM image of nanocomposite of both hydrophobic materials. The circled regions show the cluster of super hydrophobic AB nanoparticles around hydrophobic CuO-NRs, (f) SAED pattern of AB. (g) electron diffraction pattern and (h) HRTEM image of a CuO-NR.

Figure 4: (a) Raman spectra of individual AB and nanocomposite CuO-NRs/AB films. (b) Cyclic voltammetry (CV), (c) Electrochemical impedance spectroscopy measurements (EIS) and (d) typical photocurrent voltage (J-V) curves and dark current characteristics of DSSCs with as-prepared samples.

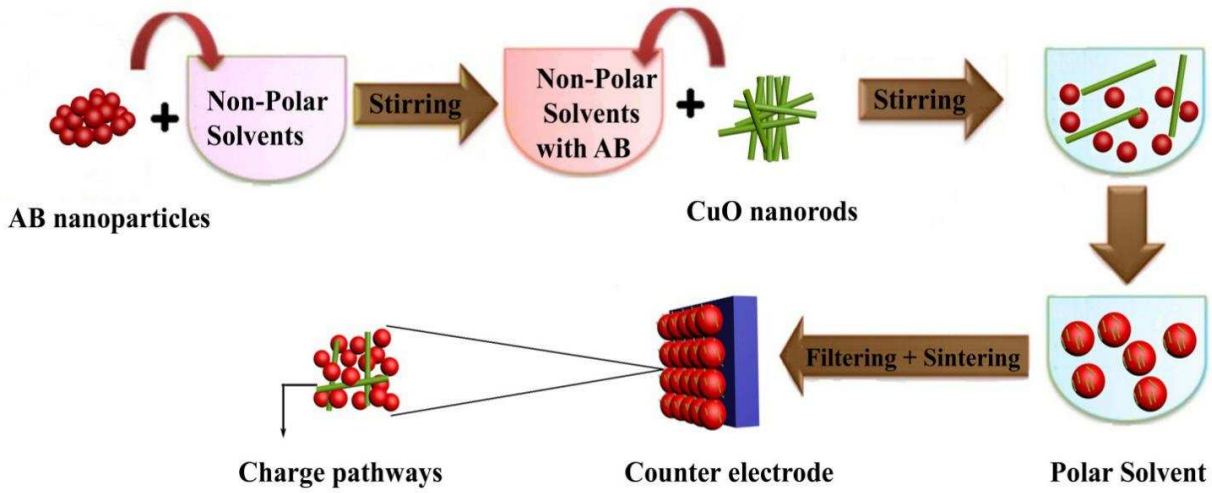

Figure 1

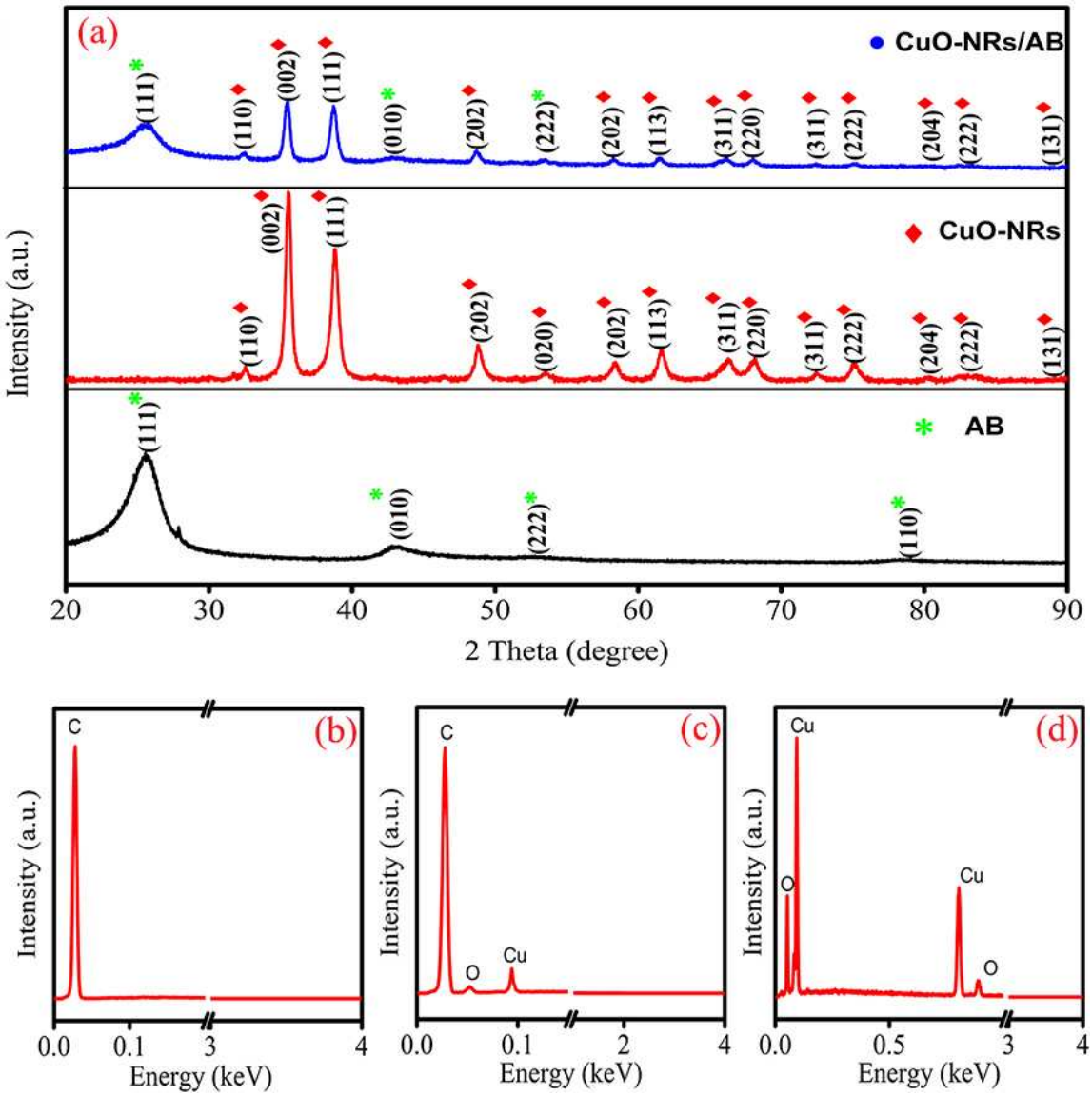

Figure 2

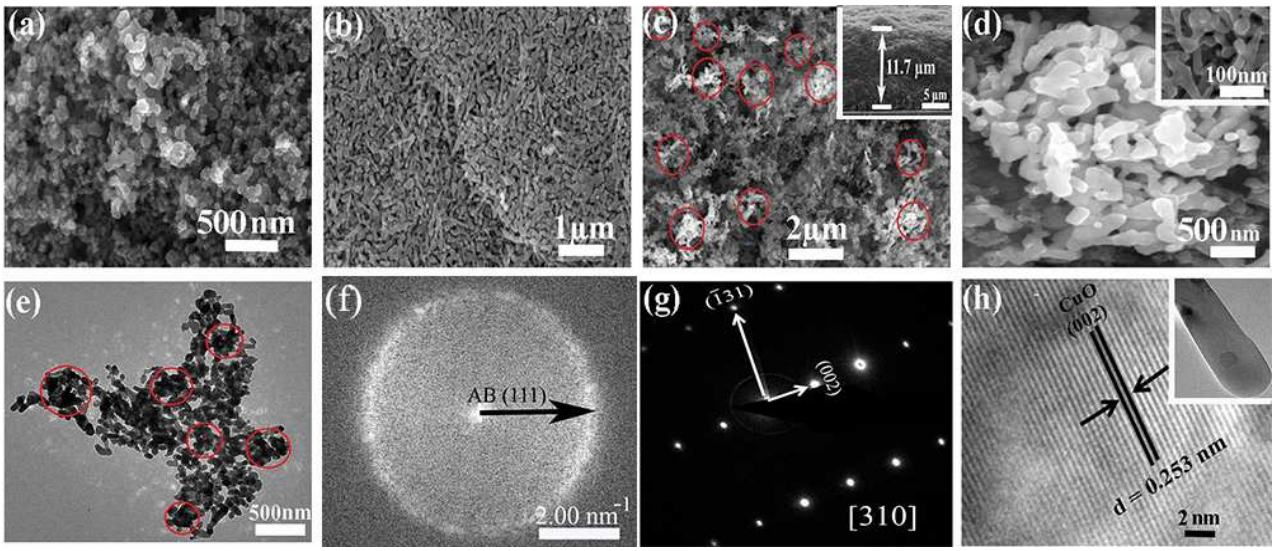

Figure 3

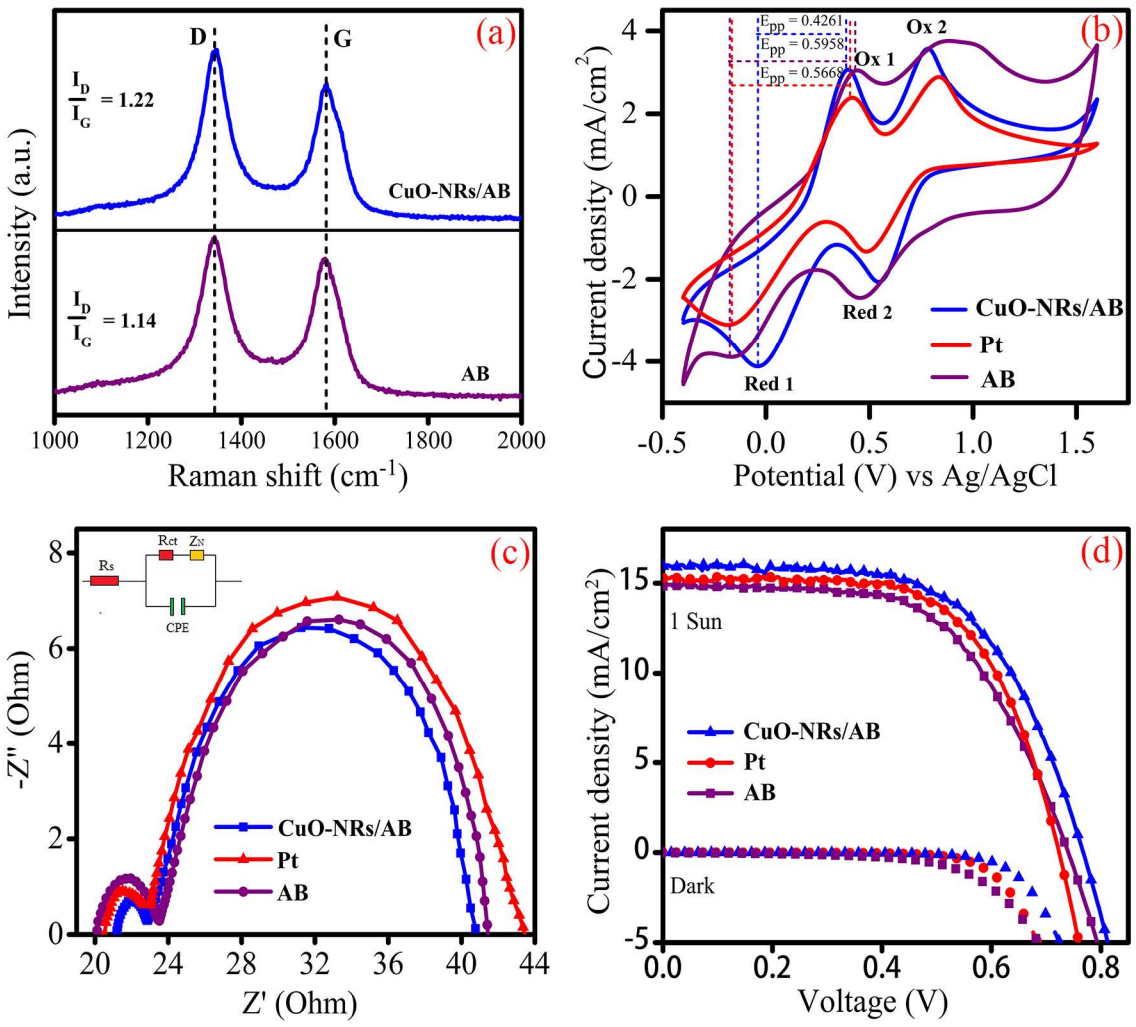

Figure 4